Type-VI and Type-V Shock-Shock Interactions on Double-Wedge Geometries Using AUSM+ on Unstructured Grid

Pabitra Halder[1], Kalyan P. Sinhamahapatra[2] and Navtej Singh[3]
[1]SM Laboratory, CSIR-CMERI, Durgapur, India
Email: p_halder@cmeri.res.in
[2]Department of Aerospace Engineering, Indian Institute of Technology, Kharagpur, India
Email: kalyanps@aero.iitkgp.ernet.in
[3]Department of Aerospace Engineering, Indian Institute of Technology, Kharagpur, India
Email: nsingh@aero.iitkgp.ernet.in

ABSTRACT
The Euler equations are solved on unstructured triangular meshes for hypersonic flow over double-wedge geometries. The driving algorithm is an upwind biased cell centered finite volume method. *AUSM+* method is used to split the fluxes. Edney (1968) studied the shock interactions by impinging an externally generated planar oblique shock on the bow shock generated by a cylinder. Depending upon the parametric conditions Edney classified the shock interactions in different types. Two interaction topologies, namely Type-VI and Type-V and the transition from Type-VI to Type-V are studied in details. Both six-shock and seven-shock configurations of Type-V interaction are presented.

Keywords: Euler solver, *AUSM+*, *MUSCL*, limiter, hypersonic double-wedge flow.

1. INTRODUCTION

When a shock wave propagating in a medium with given acoustic impedance obliquely encounters to another medium with different acoustic impedance, a reflection occurs. In the subject of shock wave reflection shock-shock interactions are very important phenomena. Shock- shock interaction phenomenon has been studied experimentally by Edney [1], where an externally generated planar oblique shock impinged on a bow shock generated by a cylinder and the two shocks interacted. Depending upon the parametric conditions, the shock interactions are classified into different types. The study has effectively shown the transition between regular and Mach reflection (*RR* and *MR*) and hysteresis phenomena in between $RR \leftrightarrow MR$. Different types of shock-shock interactions and transition from one type to the other in flow, especially, over double-wedge like geometries have been discussed in details.

Two types of shock reflections *RR* and *MR* normally occurs in steady flows as indicated by Ben- Dor [2]. If the angle of incidence (ϕ_1) is sufficiently small that the streamline deflection angle (θ_1) caused by the incident shock can be cancelled by the opposite deflection angle (θ_2) caused by the reflected shock, *RR* occurs. The condition for the *RR* is $\theta_1 - \theta_2 = 0$. In the case of *MR*, if the streamline deflection angle across the Mach stem is θ_3, the condition for *MR* is $\theta_1 - \theta_2 = \theta_3$ since the streamlines in both side of the slipstream must be parallel. On the basis of two extreme angles of incidence, namely the von Neumann angle (ϕ_1^N) and detachment angle (ϕ_1^D), the transition $RR \leftrightarrow MR$ has been explained. Theoretically, for $\phi_1 > \phi_1^D$, *RR* wave configuration is not possible, similarly for $\phi_1 < \phi_1^N$, *MR* wave configuration is not possible. In the range $\phi_1^N \le \phi_1 \le \phi_1^D$ both *RR* and *MR* wave configurations are theoretically possible and the range is known as dual-solution domain.

For asymmetric shock wave reflections, the overall *RR* wave configuration consists of two incident (i_1, i_2) and two reflected shock (r_1, r_2) waves and one slip stream. The slip stream is created due to the streamlines passing through two shocks of unequal strength. The flow deflection angles are θ_1, θ_2, θ_3 and θ_4 as the flow passes through i_1, i_2, r_1, and r_2 respectively. The condition for *RR* in asymmetric case is $\theta_1 - \theta_3 = \theta_2 - \theta_4 = \delta$. The value of δ is 0 for symmetric reflection. For MR configuration, in addition to the above incident and reflected shock waves, a Mach stem appears and it bridges two triple points and is complemented by two slipstreams. The conditions for *MR* are $\theta_1 - \theta_3 = \delta_1$ and $\theta_2 - \theta_4 = \delta_2$. For a symmetric case, $\theta_1 = \theta_2$ and $\delta_1 = \delta_2$. Analytical and experimental investigations of asymmetric shock wave reflections in steady flows have been performed by Li et al. [3]. It has been shown that a hysteresis exists in the $RR \rightarrow MR \rightarrow RR$ transition process. Three dimensional edge effects are found responsible for hysteresis. A numerical investigation on the asymmetric shock wave reflection has also been carried out by Ivanov et al. [4] and more recently a theoretical study on $RR \rightarrow MR$ transition of asymmetric shock waves in steady flows has been reported by Hu et al. [5].

In most realistic supersonic flow situations the shock-shock interactions are usually asymmetric. External flows over double-wedge like geometries fall in this category. Olezniczak et al. [6] have numerically studied inviscid shock-shock interactions on double-wedge geometries using structured mesh. Different type of shock interactions have been observed by varying the second wedge angle while keeping the first wedge angle and the ratio of the face lengths fixed. Ben-Dor et al. [7] have reported self-induced oscillations in the shock wave flow pattern formed in a stationary supersonic flow at Mach number 9 over double-wedge geometry. In their numerical investigations, self-induced oscillations and a hysteresis exist within the second wedge angle range from 41.8^0 to 43.0^0, keeping the first wedge angle and other parameters fixed.

Upwinding is the most preferred numerical scheme for high-speed flow simulation. Upwind schemes are usually categorized as either Flux Difference Splitting (FDS) or Flux Vector Splitting (FVS). The most successful and popular approximate Riemann solver (FDS) is Roe's method, which is the exact solution of a linearized Riemann problem (Roe [8]). It is able to capture stationary discontinuities with no numerical dissipation. However, at strong expansions, the Roe scheme tends to diverge even if the entropy fix is applied. In addition, FDS scheme suffers from the so called "carbuncle phenomenon" – a numerical instability in capturing strong shock waves in multidimensional computations.

Other way of introducing upwind is FVS, in which the numerical flux function is divided into positive and negative parts. Steger and Warming [9] made use of similarity transformations and the homogeneity property of the Euler equation, in splitting the flux depending on the sign of the eigenvalues of the flux Jacobian matrix. However, this splitting has problem around the sonic point, and van Leer [10] proposed an alternative splitting, which gives noticeably better results.

These FVS schemes share a serious disadvantage: large dissipation on contact discontinuities and shear layers.

A more recent effort to develop less-dissipative upwind schemes focuses on reducing the surplus dissipation of the FVS by introducing the flavor of FDS into FVS schemes. Liou and Steffen [11] proposed a promising scheme named Advection Upstream Splitting Method (AUSM) (Fezoui and Stroufflet [12]) in which the cell-face advection Mach number is appropriately defined to determine the upwind extrapolation for the convective quantities. The $AUSM^+$ (Liou [13]) is designed to be a further improvement of AUSM, and offers further improvement in accuracy over its predecessor (AUSM) and other popular schemes, simplicity, and easy generalization to other conservation laws.

The desire to compute flows over complex geometrical body, the widely used multi-block structured grid approach can be used. But the automation of the blocking and grid generation process is difficult tasks that are continually being refined. The unstructured grid can be used for this kind of problem as well as simple geometrical problem (Venkatakrishnan [14]; Bertolazzi and Manzini [15]; Batina [16]; Jameson and Mavriplis [17]).

In the present study the two-dimensional Euler equations are solved on unstructured triangular meshes to study the shock interactions in high Mach number flow over double-wedge excluding the self-induced oscillations regime (Ben-Dor et al. [7]) in the shock wave flow pattern. The driving algorithm is an upwind biased cell-cantered finite volume method. The spatial discretization involves a naturally dissipative flux-split approach that sharply captures shockwaves.

1.1 Statement of the Problem

The hypersonic flow over double-wedge geometry is schematically shown in the Figure 1. Considering a calorically perfect diatomic gas, the ratio of specific heats (γ) is fixed at 1.4. The free stream Mach number (M_∞) is taken as 9.0. The ratio of the first face length to the second face length (L_1/L_2) is kept at 1. The first wedge angle (θ_1) is taken 15°. Keeping all these parameters fixed, the second wedge angle (θ_2) is gradually increased from 35° to 45° to explore the two-dimensional M, θ_2, parameter space with regard to shock interactions. The shock interactions are presented in order of occurrence with increase in the second wedge angle. Since, the problem is symmetric, only half of the flow field, with respect to the symmetric line marked in figure 1, is taken as the computational domain. In the present calculations, free stream values for density, pressure and velocity are assigned as the initial values to each triangular cell in the domain. The free stream flow conditions are selected as $P_\infty = 170$ Pa and $\rho_\infty = 0.002$ Kg/m^3.

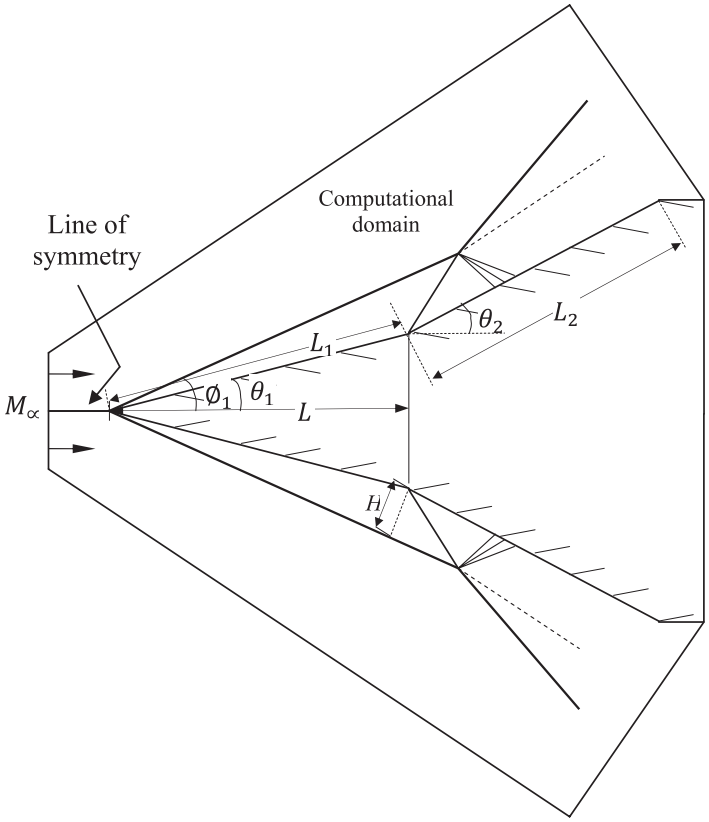

Figure 1. Flow geometry.

2. FORMULATIONS AND NUMERICAL METHODS

2.1 Solution of the two dimensional governing equations

In the present study, the flow is assumed to be governed by the two-dimensional Euler equations where the variables to be determined are the density, Cartesian velocity components, pressure and total energy per unit volume, denoted respectively by ρ , u, v, p and e. The two dimensional Euler equations in integral form can be written as follows:

$$\frac{\partial}{\partial t}\iint_{\Omega} Q dV + \oint_{\partial\Omega} \left(n_x F + n_y G\right) dS = 0 \tag{1}$$

where the vector of conserved variables Q, inviscid flux vectors F, G are given below,

$$Q = \begin{Bmatrix} \rho \\ \rho u \\ \rho v \\ e \end{Bmatrix}, F = \begin{Bmatrix} \rho u \\ \rho u^2 + p \\ \rho uv \\ (e+p)u \end{Bmatrix}, G = \begin{Bmatrix} \rho v \\ \rho vu \\ \rho v^2 + p \\ (e+p)v \end{Bmatrix} \tag{2}$$

and the pressure p is given by the equation of state for a perfect gas, namely

$$p = (\gamma - 1)\left\{e - \tfrac{1}{2}\rho(u^2 + v^2)\right\} \tag{3}$$

In equation (1), Ω denotes the domain of computation that is bounded by $\partial\Omega$, n_x and n_y are the x- and y- components of the outward unit normal to the differential surface dS. The integrand namely inviscid fluxes of mass, momentum and energy of a control volume can be rewritten as,

$$F_{ed} = n_x F + n_y G = V_n \begin{Bmatrix} \rho \\ \rho u \\ \rho v \\ e + p \end{Bmatrix} + p \begin{Bmatrix} 0 \\ n_x \\ n_y \\ 0 \end{Bmatrix} \tag{4}$$

where, $V_n = un_x + vn_y$ is the convective velocity normal to the face.

The semi-discretized form of the equation (1) over a control volume (*CV*) containing *'Nedge'* number of edges can be written as,

$$\frac{d}{dt}\left(Q_j A_j\right) + \sum_{m=1}^{Nedge} F_{ed\,m} \Delta S_m = 0 \tag{5}$$

where A_j is the area of control volume (*CV* number *'j'*). The subscript *'m'* indicates the local face number of *CV* numbered *j*. The maximum number of edge of the *CV* is indicated by '*Nedge*'. The inviscid flux vector is computed using the *AUSM+* flux-vector splitting with MUSCL-type upwind-biased interpolation scheme.

2.2 AUSM⁺ flux splitting

The *AUSM* + is a hybrid method of spatial discretization. In this method flux vectors are split into forward and backward contributions, which are continuously differentiable even at sonic and stagnation points. As a first step in formulation of the $AUSM^+$ method, the convection and acoustic waves are recognized as two physically distinct processes. The flux (F_{ed}) at the interface of two neighbor cells (edge) is written as a sum of the numerical convective flux and the numerical pressure flux.

$$F_{ed} = F_{ed}^{c} + P_{ed} \tag{6}$$

where,

$$F_{ed}^{c} = m_{ed} a_{ed} \Phi_{\mathrm{ed}}, \quad \Phi_{\mathrm{ed}} = (\rho, \rho u, \rho v, h)^{\mathrm{T}} \tag{7}$$

a_{ed} is an interface numerical speed of sound and $h = e + p$. a_{ed} is determined using an arithmetic average of left (l) and right (r) states as

$$a_{ed} = \frac{a_l + a_r}{2} \tag{8}$$

$$P_{ed} = \begin{Bmatrix} 0 \\ p_{ed} \\ 0 \\ 0 \end{Bmatrix} \tag{9}$$

The interface Mach number a_{ed}, is written as sum of two individual components,

$$m_{ed} = M^{+}(M_l) + M^{-}(M_r) \tag{10}$$

The "+" and "-" are understood to be associated with the right and left-running waves. Here, M_l and M_r are determined as,

$$M_l = \frac{\vec{V_l}.\vec{n}}{a_{ed}}, \qquad M_r = \frac{\vec{V_r}.\vec{n}}{a_{ed}} \tag{11}$$

The split Mach numbers ($M^{\pm}$) are defined as,

$$M^{\pm} = \begin{cases} \frac{1}{2}(M \pm |M|), if\ |M| \geq 1 \\ M_{\beta}^{\pm}(M), otherwise \end{cases} \tag{12}$$

with

$$M_{\beta}^{\pm}(M) = \pm\frac{1}{4}(M \pm 1)^2 \pm \beta(M^2 - 1)^2, -\frac{1}{16} \leq \beta \leq \frac{1}{2} \tag{13}$$

The interface pressure is written as

$$p_{ed} = P^{+}(M_l)p_l + P^{-}(M_r)p_r \tag{14}$$

where the split pressures are given by

$$P^{\pm}(M) = \begin{cases} \frac{1}{2}\left(1 \pm sign(M)\right), & if\ |M| \geq 1 \\ P_{\alpha}^{\pm}(M), & otherwise \end{cases} \tag{15}$$

with

$$P_{\alpha}^{\pm}(M) = \frac{1}{4}(M \pm 1)^2(2 \mp M) \pm \alpha M(M^2 - 1)^2, \qquad -\frac{3}{14} \leq \alpha \leq \frac{3}{16} \tag{16}$$

Full upwinding of both pressure and Mach number is achieved for supersonic flow; whereas a polynomial blending of upstream and downstream contributions are obtained for subsonic flow. The numerical flux normal to a cell interface is obtained by assembling the two contributions as,

$$F_{ed} = [F_{ed}^{c+}(q^-) + P_{ed}^{+}(q^-) + F_{ed}^{c-}(q^+) + P_{ed}^{-}(q^+)] \tag{17}$$

The fluxes are evaluated by *MUSCL* (Monotonic Upstream-centered Scheme for Conservation Laws) type reconstruction of the primitive variables q at the cell faces.

2.3 Flux computation on unstructured grid

A cell centered scheme is adopted where the flow variables are stored at the centroid of each triangle and the control volume is the triangle itself. The scheme is derived as follows.

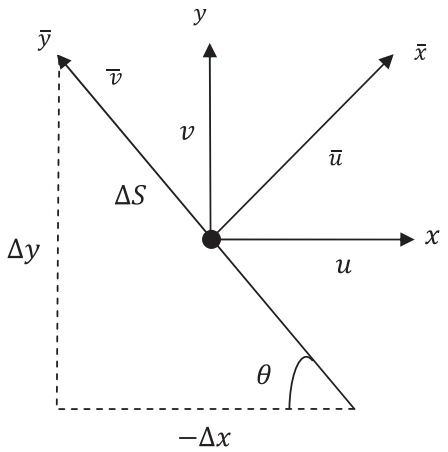

Figure 2. Directed edge and velocity components normal and along the edge.

The flux across a face is obtained as $F_{ed}\,\Delta S = F\Delta y - G\Delta x$. For each edge of a given triangle, the fluxes are first rotated into a locally Cartesian co-ordinate system $\bar{x}$ and $\bar{y}$ with the principal direction being perpendicular to the edge as shown in figure 2. The flux in this direction is defined as

$$H\Delta S = T(F\Delta y - G\Delta x) = [\rho\bar{u}, \rho\,\bar{u}^2 + p, \bar{u}\bar{v}, e\bar{u} + p\,\bar{u}]^T \tag{18}$$

where T is the transformation matrix, Δx and Δy are the directed lengths of the edge and $\Delta S^2 = \Delta x^2 + \Delta y^2$.

Here, $\bar{u}$ and $\bar{v}$ are the velocity components perpendicular and parallel to the edge and are given by,

$$\bar{u} = u\frac{\Delta y}{\Delta s} - v\frac{\Delta x}{\Delta s}$$
$$\bar{v} = u\frac{\Delta x}{\Delta s} + v\frac{\Delta y}{\Delta s} \tag{19}$$

The flux vector H is split in a one-dimensional fashion into forward (H^+) and backward (H^-) components by using the *AUSM+* flux splitting method. The resulting split fluxes are finally rotated back into the original coordinate system, so that

$$(F\Delta y - G\Delta x) = T^{-1}[H^+(q^-) + H^-(q^+)]\Delta s \tag{20}$$

To increase the order of spatial accuracy a *MUSCL*-type approach is used to interpolate the variables at the edges.

For a triangle *j*0 (centroid at *j*0) the upwind biased interpolation for q^- along the edge *e*1 delimiting the triangles *j*0, *j*1 is defined by,

$$q^- = q_{j0} + \frac{1}{4}[(1-\kappa)\delta_- + (1+\kappa)\delta_+] \tag{21}$$

where, $\delta_+ = q_{j1} - q_{j0}$
$\delta_- = q_{j0} - q_{i3}$

q_{j0} and q_{j1} are the vectors of primitive variables at the centrods *j*0 and *j*1 respectively and q_{i3} is the vector of primitive variables at node *i*3, the third vertex of the *CV*. The upwind biased interpolation for q^+ is also obtained in a similar fashion by considering flow variables at the two centroids (*j*0 and *j*1) and node *i*4, the third vertex of the element whose centroid is *j*1. The parameter k is the controlling factor that gives rise to different schemes by appropriately weighting δ^- and δ^+. The value of k is taken 1/3 which leads to a third order accurate upwind- biased scheme for one-dimensional computations. The formulae for δ^- and δ^+ are modified to account for the distances from the midpoint of the directed edge to the centroids of the delimiting triangles to weight the flow variables appropriately. To control the numerical oscillations in the regions of high gradients (e.g., at shocks), usually associated with upwind-biased schemes, the min-mod limiter is used.

2.6 Temporal discretization

The time integration is performed by approximating the time derivative as,

$$\frac{\partial Q}{\partial t} = \frac{2+\varphi}{2}\frac{\Delta Q}{\Delta t} - \frac{\varphi}{2}\frac{Q^n - Q^{n-1}}{\Delta t} \tag{22}$$

where, $\Delta Q = Q^{n+1} - Q^n$. The parameter φ controls the order of temporal accuracy. In the present calculation φ is taken to be 1 which gives a second order accuracy in time.

The local time step for each cell in the mesh is calculated using the following relationship,

$$\Delta t = \frac{CFL.\Delta S_{min}}{\sqrt{u^2+v^2}+a} \tag{23}$$

where, ΔS_{min} is the characteristic length scale of the cell, taken as the minimum face length of the triangular element. The minimum of all the local time steps is selected as Δt. An appropriate choice of the *CFL* number is used to ensure stability. The triangles of the unstructured mesh are recorded in a particular fashion from upstream to downstream and the solution is obtained by sweeping from upstream to downstream.

2.7 Boundary conditions

The flow tangency condition on the wall is imposed using dummy cells. The velocity components within a dummy cell are determined from the values in the cell adjacent to the boundary surface such that the normal component is zero on the surface. The velocity in the dummy cell is given by

$$\begin{bmatrix} u_d \\ v_d \end{bmatrix} = \begin{bmatrix} 1-2n_x^2 & -2n_x n_y \\ -2n_x n_y & 1-2n_y^2 \end{bmatrix} \begin{bmatrix} u_j \\ v_j \end{bmatrix} \tag{24}$$

The values of density and pressure in a dummy cell are set equal to the respective values at the adjacent cell.

A characteristic based analysis using the fixed and extrapolated Riemann invariants is implemented to calculate the values of the flow variables in a cell on the outer boundary. For supersonic inflow or outflow, the locally one-dimensional Riemann invariants and entropy, i.e.

$$\begin{aligned} R_1 &= \vec{V}.\hat{n} - \frac{2a}{(\gamma-1)} \\ R_2 &= \vec{V}.\hat{n} + \frac{2a}{(\gamma-1)} \\ R_3 &= \frac{p}{\rho^{\gamma}} \end{aligned} \tag{25}$$

are computed respectively from outside or inside the computational region. For subsonic inflow R_1 and R_3 are given from outside and R_2 from inside and for subsonic outflow R_2 and R_3 are calculated from inside and R_1 from outside.

3 RESULTS AND DISCUSSION

Type-VI and Type-V shock interactions in flow over double-wedge configuration at free stream Mach number 9 is studied here. The air is considered a perfect gas with γ= 1.4. The ratio of the wedge face lengths (L_2/L_1) and the first wedge angle (θ_1) are respectively kept fixed at 1.0 and 15^0. The second wedge angle θ_2 is varied within the range of 35^0 to 45^0. The different flow topologies and characteristics of shock-shock interactions are presented in order of occurrence as θ_2 increases. The discussion is split into two subsections – Type-VI and Type-V shock interactions. The constituent elements of the structure of the Type-VI and Type-V are discussed in details. All linear dimensions are normalized with the first wedge length (*L*), the horizontal component of the face length. Local refinement is used near the wedge surface and corner to resolve the large and rapid changes in the flow properties in these regions.

3.1 Type-VI interactions

With fixed free stream conditions and other parameters (γ, θ_1 and L_2/L_1), the interactions topology of the two leading shock waves generated from the two leading edges of the double- wedge geometry solely depends on the difference of the two wedge angles ($\Delta\theta = \theta_2 - \theta_1$). With relatively small $\Delta\theta$ the interaction of the two leading shock waves of the same family belongs to Type-VI interaction. The Type-VI wave configuration is schematically shown in figure 3. The flow field consists of two incoming shock waves (IS1 and IS2) created from the leading edges and two outgoing waves separated by a contact discontinuity or slip line (Cd).

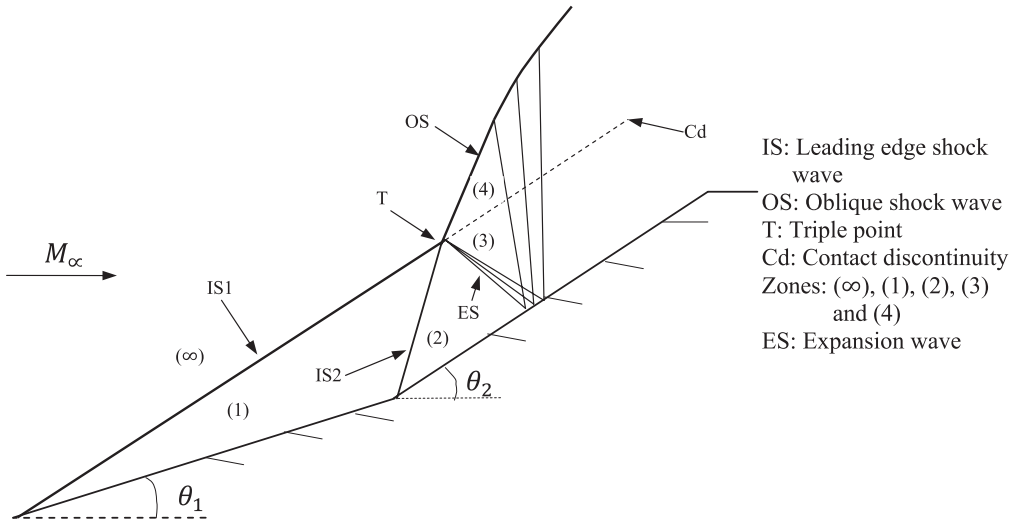

Figure 3. Schematic diagram of a Type-VI shock interaction.

These two incoming waves, two outgoing waves and the slip line meet at a single interaction point named as triple point (T). The outgoing waves consist of a transmitted shock wave (OS) and an extra wave (ES) which reflects from the second wedge surface. This extra wave is normally an expansion wave but for some cases it might be a shock wave depending upon the flow conditions and first wedge angle. The contact discontinuity separates the fluid that has passed through both the incoming shock waves (IS1 and IS2) from the fluid that only passed through the transmitted shock wave (OS). For shock interaction Type-VI, one of the major criteria is that the total flow field is supersonic. For completeness of understanding, a schematic diagram of the shock polar for Type-VI interaction in a hypersonic flow with $M_\infty = 9$, $\theta_1 = 15^0$ and $\theta_2 = 35^0$ is shown in figure 4.

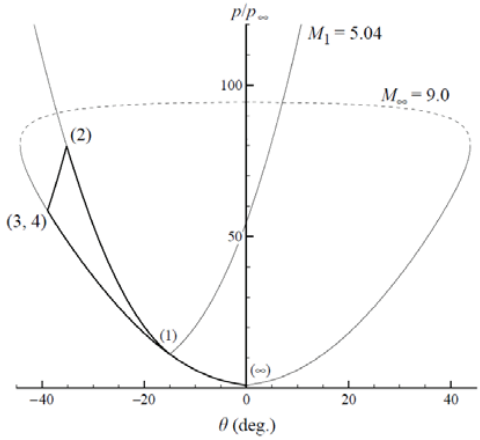

Figure 4. Shock polar diagram for a Type-VI shock interaction with θ_1 = 15° and θ_2 =35°

About the interaction point (T in figure 3), the overall flow field is divided into five regions marked as (1), (2), (3), (4) and (∞) by five discontinuities and the regions are marked in the schematic diagram (figure 3) and shock polar (figure 4). Since the flow after an oblique shock is parallel to the wedge surface, Point 1 for region (1) and Point 2 for region (2) in the shock polar diagram are located at $\theta = -15^0$ and $\theta = -35^0$ (using Edney's angle convention) respectively. The location of Point 1 on the

shock polar diagram is on the free stream Mach number 9. With the fixed pressure ratio, the Mach number (M) at region (1) is uniquely determined and the value is 5.04. The polar for region 1 is now drawn from Point 1. The Point 2 is located on the shock polar of M = 5.04 at $\theta = -35^0$. The locations of Points 3 and 4 can be determined in the shock polar diagram by gas dynamic consideration. The Point 4 must lie on the M = 9 polar. Since regions (3) and (4) are separated by only a contact discontinuity; Point 3 also lies at the same location of Point 4. In between the regions (2) and (3), there is a Prandtl-Meyer expansion fan. The Points 3 and 4 lie on the intersection of the isentropic expansion path originated from Point 2 and the M = 9 polar (θ_{ip}). The summery of shock location points in the shock polar diagram is shown in Table 1.

Table 1. Shock polar locations for different wave configurations

Points in Shock Polar	Regions in Wave Configuration	θ,M
1	(1)	-15, 9.0
2	(2)	-35, 5.04
3, 4	(3), (4)	θ_{ip} , 9.0

The exploded view of the mesh near the corner of the double-wedge is shown in figure 5. The grid contains 113049 nodes and 225134 triangular elements. The grid spacing in this problem introduces a very critical length scale that determines the capturing of the shock-shock interaction. Consequently, a very fine mesh surrounding the triple point is required. This is achieved with the help of local refinement at and about the corner point and triple point. With the help of local refinement of an unstructured grid, the shock-shock interactions are captured accurately with considerably less number of cells (unknown variables). In this respect, the unstructured Euler solver is very convenient compared to any structured solver where multi- block grid structure with very high level of refinement is obvious. For solving this particular problem Olejniczak et al. [6] used grid sizes of 1024 × 1024 points while many features in some of the interactions were lost in a 512 × 512 mesh. However, almost similar accuracy is obtained here with a mesh that contains only about 20% unknowns.

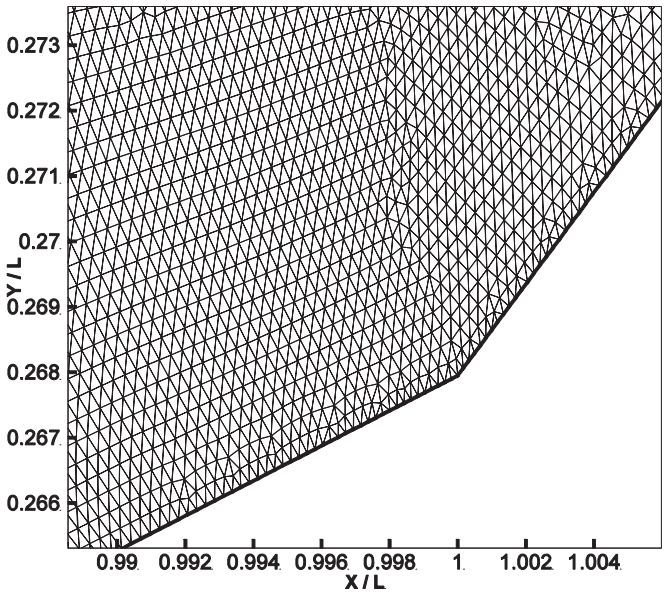

Figure 5. Exploded view of the mesh near the corner.

Figures 6a-c show the wave configurations for Type-VI shock interactions. The Mach contours presented in figure 6b clearly show that the whole flow field is supersonic. A contact discontinuity is distinctly seen in the Mach contours and density contours. It is clear from the figure 6b, that the flow velocity below the contact discontinuity (region 3) is higher than the velocity above the contact discontinuity (region 4). On the other hand figure 6a shows that the pressure in regions above and below the slip line (contact discontinuity) is continuous. An expansion fan is also created from the intersection point of two shocks and is reflected back from the surface of the second wedge and slightly deflects when it passes through the contact discontinuity. This is visible in the pressure contours (figure 6a). The normalized pressure jump through the first oblique shock (IS1) is found to be 11.18, which matches well with the theoretical value of 11.2. For the second oblique shock (IS2) the computed pressure jump is 80.17. In the contact discontinuity regions (3) and (4), the value is found 47.2. Some discrepancies with the theoretical value have been found in this region due to the presence of the expansion waves.

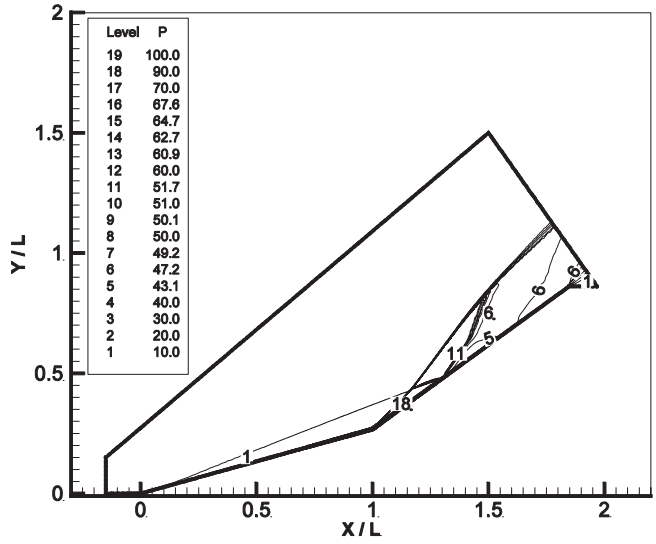

a. Pressure contours

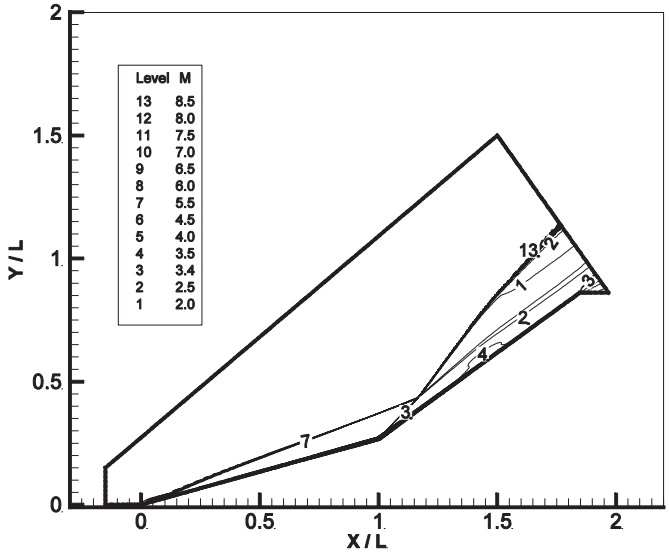

b. Mach contours

Figure 6 (Continued)

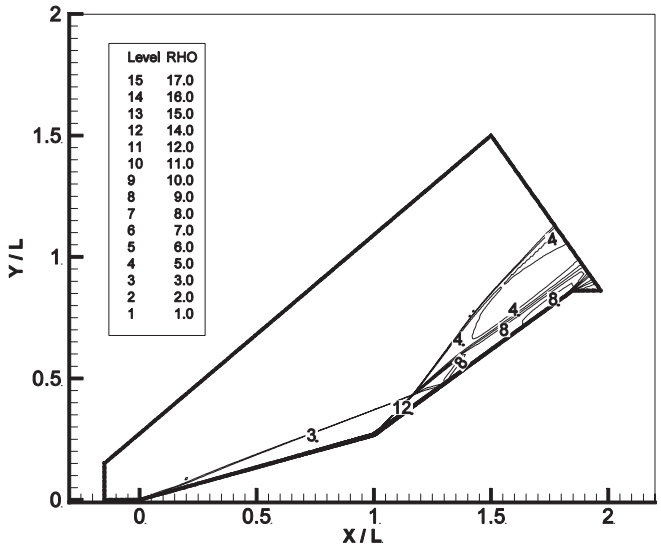

c. Density contours

Figure 6. The contours of (a) Pressure, (b) Mach number and (c) Density for a Type-VI interaction with $\theta_2 = 35^0$.

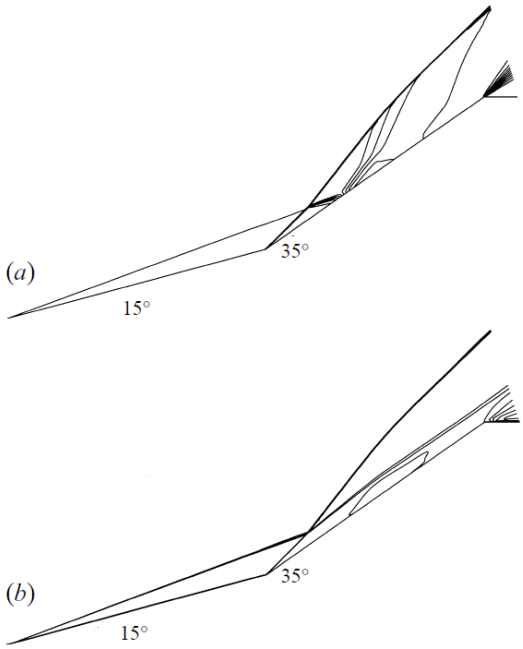

Figure 7. (a) Pressure contours, and (b) Mach number contours for a Type-VI interaction with $\theta_2 = 35^0$. (Olejniczak et al., [6]).

The pressure and Mach number contours for the same flow configuration as given by Olejniczak et al. [6] are reproduced in figure 7. The two results are found to match quite closely. The computed normalized surface pressure for a Type-VI interaction is shown in the figure 8. The maximum normalized surface pressure on the first wedge is found 11.2 due to the oblique shock generated at the

nose of the first wedge. The peak in the computed surface pressure, at a pressure ratio of about 90, is due to the second oblique shock generated from the corner of the double- wedge at $\theta_2 = 35^0$.

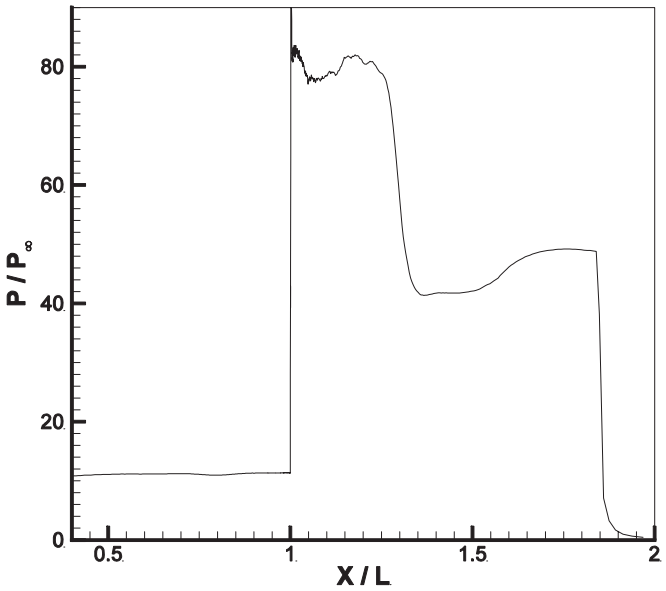

Figure 8. Surface pressure for a Type-VI interactions with $\theta_2 = 35^0$.

In the shock polar (figure 4) the Points 3 and 4 lie below the sonic point of the free stream polar. Now, at fixed first wedge angle $\theta_1 = 15^0$), if the second wedge angle θ_2 increases, the Point 2 moves up and left on the shock polar diagram. As a result, above certain θ_2, the expansion wave originating from Point 2 intersects the free stream polar above its sonic point and the purely supersonic Type-VI interaction can no longer exist. This is the transition criteria from Type-VI to Type-V. The transition process from Type-VI to Type-V interaction occurring over a small change of θ_2 has been shown with the help of contours of pressure and Mach number in figures 9, 10 and 11. The results are shown over a small range of second wedge angles (39.5^0, 40.0^0 and 41.0^0) where the transition is found to occur. At the second wedge angle of 39.5^0, there is still pure supersonic flow which is clear from the contours of Mach number (figure 9b). The maximum normalized pressure shown in contours of pressure is below 110 which is one of the criteria for Type-VI shock interactions at Mach 9.

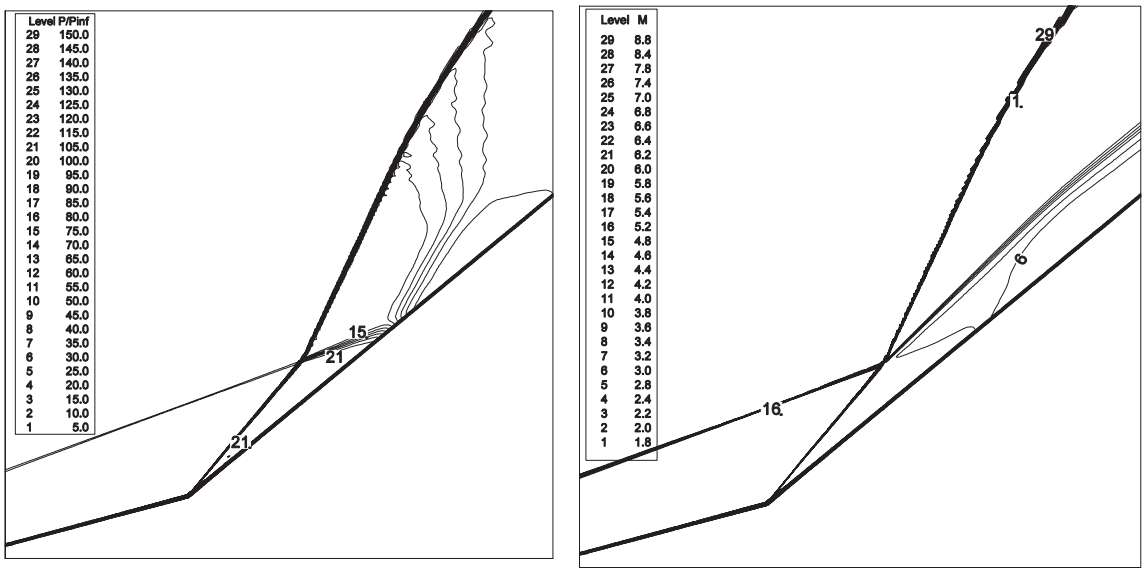

(a) Contours of pressure (b) Contours of Mach number

Figure 9. Contours of pressure and Mach number at $\theta_2 = 39.5^0$.

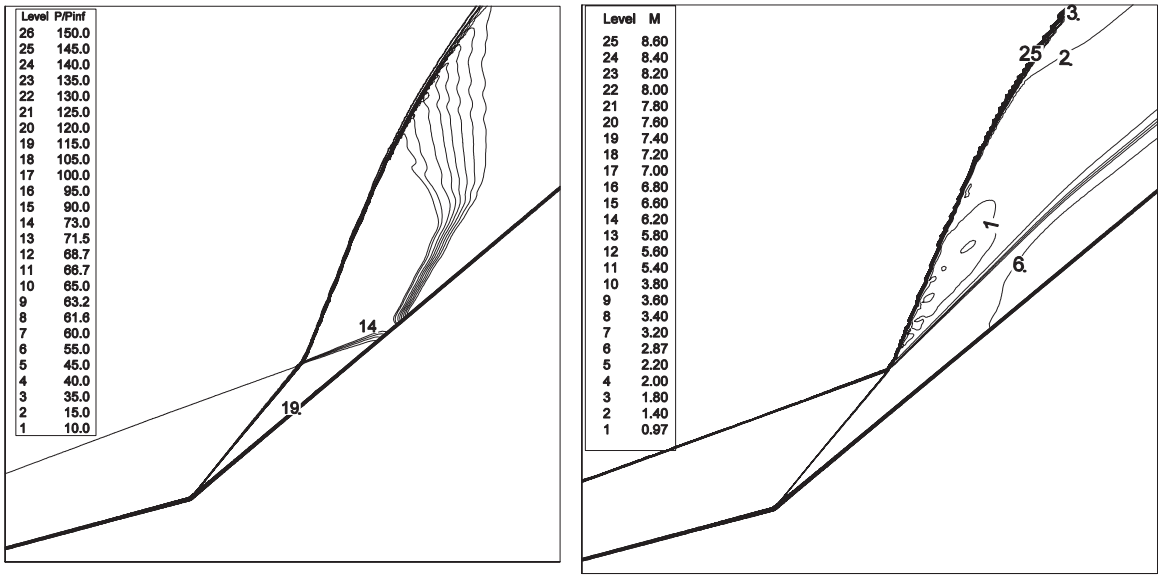

(a) Contours of pressure (b) Contours of Mach number

Figure 10. Contours of pressure and Mach number at $\theta_2 = 40.0^0$.

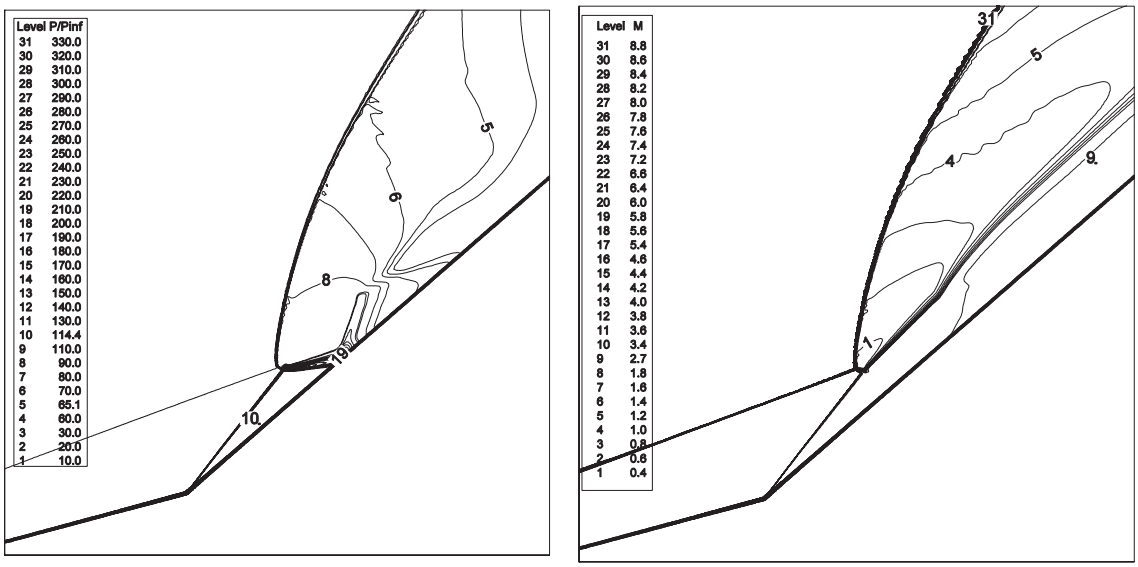

(a) Contours of pressure (b) Contours of Mach number

Figure 11. Contours of pressure and Mach number at $\theta_2 = 41.0^0$.

When θ_2 is increased to 40^0, the corresponding Mach contours, shown in figure 10b, clearly reveals the appearance of a very small subsonic zone (just below Mach 1.0). From the contours of pressure (figure 10a), the maximum normalized pressure is seen to be higher than 110. Thus, at $\theta_2 = 40^0$, the shock interaction does not belong to Type-VI interaction. The transition occurs in between 39.5^0 and 40.0^0 of the second wedge angle. This transition θ_2 has been predicted by Olejniczak et al. [6] to be 39.76^0 . It can be fairly concluded that present numerical scheme correctly predicts the transition in shock interaction. By keeping all the parameters same, the second wedge angle is now increased to 41^0. The contours of pressure and Mach number (figures 11a-b) show a shock interaction of Type-V. A large subsonic zone near the triple point is visible in figure 11b and the maximum normalized pressure is about 210 as shown in figure 11a. The details of Type-V shock interaction and its development are discussed in the next subsection.

3.2 Type-V interactions

With a given first wedge angle θ_1, above a certain value of second wedge angle θ_2 (as discussed in the previous section), the interaction undergoes a change in pattern, i.e., Type-VI to Type-V. The key feature in a Type-V interaction is that there must be subsonic zones after the reflection of two oblique shock waves of opposite families. The Type-V shock interaction normally consists of either a six-shock structure or a seven-shock structure. When the second wedge angle θ_2 is little higher than the Type-VI to Type-V transitional value the six-shock Type-V interaction occurs. This six-shock type interaction normally occurs with a steady regular wave configuration. As the second wedge angle θ_2 further increases the flow topology changes from six-shock to seven-shock Type-V interaction with Mach reflection (MR) configuration. The flow features of these two structures of Type-V are explained with the help of schematic diagrams. Two-possible flow topologies (six-shock and seven-shock Type-V) with complete notations for the major elements of the shock interaction structures are shown in figure 12a-b. Figure 12a illustrates the six-shock Type-V interaction. It is composed of one triple-shock sub-structure and a regular interaction sub-structure denoted by T_u and I_p respectively. The triple-shock structure contains three shock waves denoted by IS1 (created from first wedge leading

edge), the bow shock wave OSB and MWS (Mach stem), and a contact discontinuity denoted by Cd1 emitted from T_u. In the regular interaction substructure, four shock waves denoted by IS2 (generated from the leading edge of the second wedge), MWS, SW1 (meets Cd1) and SW2 (reflected shock wave from the second wedge surface) meet at a point (I_p). An expansion fan (generated from the meeting point of SW1 and Cd1) is also shown in the schematic diagram. The different zones are indicated by (∞), (1), (2), (3), (4), (5) and (6) respectively.

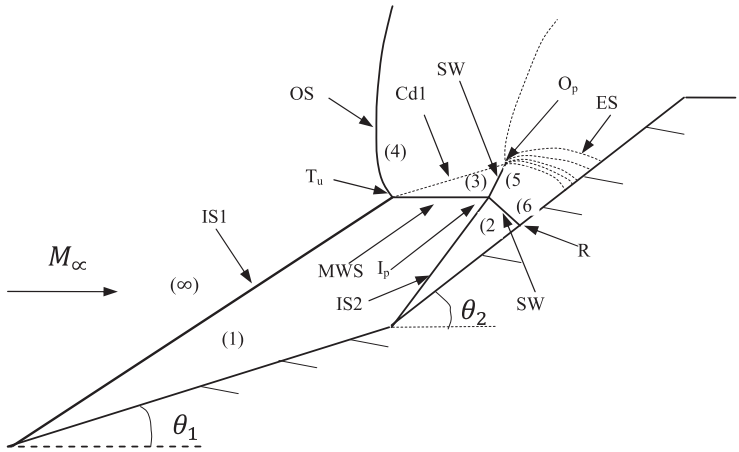

(a) Six-shock configuration of Type-V interaction

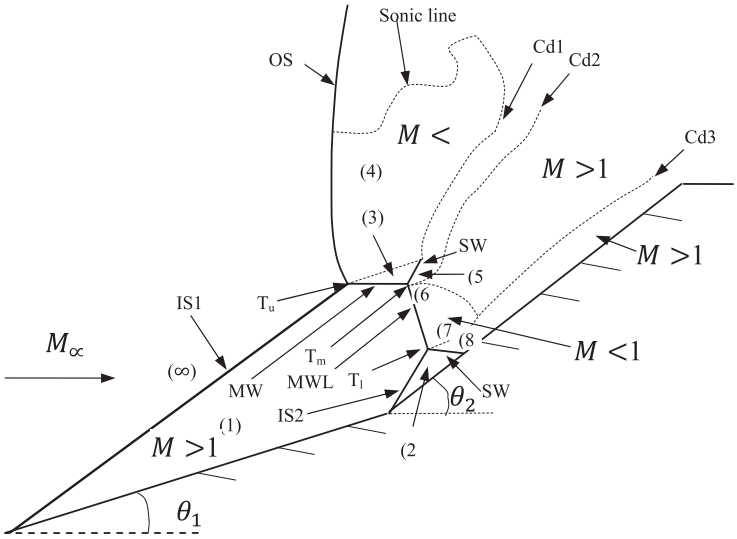

(b) Seven-shock configuration of Type-V interaction

Figure 12. Schematic diagram for the Type-V shock-shock interaction and notations used

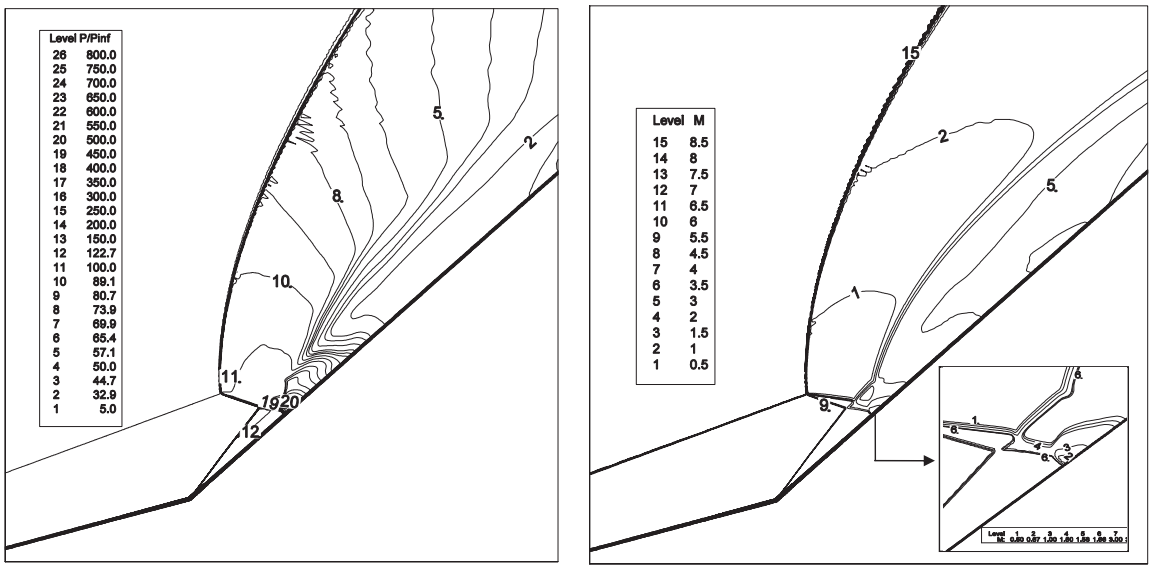

(a) Contours of pressure (b) Contours of Mach number

Figure 13. Contours of pressure and Mach number at $\theta_2 = 41.5^0$.

The detail of a typical seven-shock structure is shown in figure 12b. Instead of the single triple shock structure in a six-shock configuration, it contains three triple shock structures denoted by T_u (Upper triple point), T_m (intermediate triple point) and Tl (lower triple point). Each of these triple points contains three shock waves and a contact discontinuity as shown in the schematic diagram. In the seven-shock Type-V interaction, there are two Mach stems denoted by MWU (connected to T_u and T_m) and MWL (connected to T_m and T_l). The contact discontinuity surfaces are marked as Cd1 (generated from T_u), Cd2 (generated from Tm) and Cd3 (generated from T_l). The important flow zones are indicated in the schematic diagrams.

Using the same free stream flow conditions and the first wedge angle ($\theta_1 = 15^0$), a six-shock structured Type-V interaction has been obtained at $\theta_2 = 41.5^0$. The computational results are shown in figure 13a-b. The flow zones and the interacting shock structure depicted in the schematic diagram are clearly seen in the computed contour diagrams. Downstream of the Mach stem (MWS) a small supersonic zone (3) is present, which is separated by a contact discontinuity (Cd1) from a large subsonic zone (4) between OSB and Cd1. A very small subsonic pocket (6) is visible in the downstream of the shock (SW2) reflection point on the second wedge surface (R_p). It is shown in the enlarged view in the lower right corner of figure 13b. The shock wave SW1 meets the contact discontinuity and the interaction causes a series of expansion waves to emit from the point, which reaches the surface of the second wedge (visible in the contours of pressure in figure 13a). As a result the subsonic flow behind SW2 matches with the downstream supersonic flow. Consequently, it can be said that a convergent-divergent stream tube (subsonic- sonic-supersonic) is formed between the contact discontinuity and second wedge surface. The contours of pressure (figure 13a) show that the maximum normalized pressure for this six-shock Type-V interaction is about 500 in the zone (6), 0.103*L* away from the corner.

Figure 14a-b illustrates the seven-shock Type-V interaction. The numerical results are obtained with the second wedge angle increased to 45^0. The contours of Mach number in figure 14b show a region bounded by the two contact discontinuities (Cd1 and Cd2 according to the schematic diagram 12b) created from the upper and intermediate triple points (T_u and T_m). This region actually carries jet like properties, so it is termed a jet. Similarly, a convergent-divergent nozzle type flow behavior is visible in the Mach number and pressure contours behind the lower Mach stem (MWL). Behind the MWL and bounded by the two contact discontinuities (Cd2 and Cd3), a large subsonic zone is visible in the

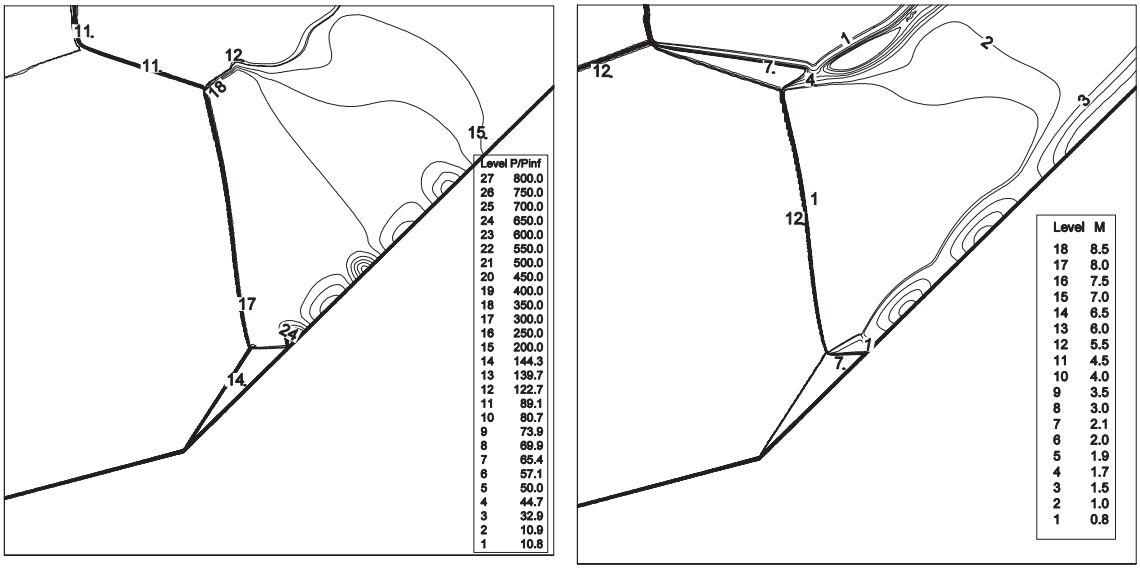

(a) Contours of pressure (b) Contours of Mach number

Figure 14. Contours of pressure and Mach number at $\theta_2 = 45^0$.

contours of Mach number. When the flow moves downstream within this two contact discontinuities, it gradually becomes supersonic to match with the outflow. As a result, a subsonic-supersonic transition process takes place and the region is termed as convergent-divergent nozzle whose throat is actually the sonic line in Mach number contours and the two contact discontinuity lines are the two blades of that convergent-divergent nozzle. The contours of pressure near the second wedge surface show a series of alternating isentropic expansion and compression waves. Similar flow feature normally occurs in an underexpanded jet. The numerical normalized pressures, 11.18 in the region (1) and 144.30 in the region (2) agree well with the analytical results.

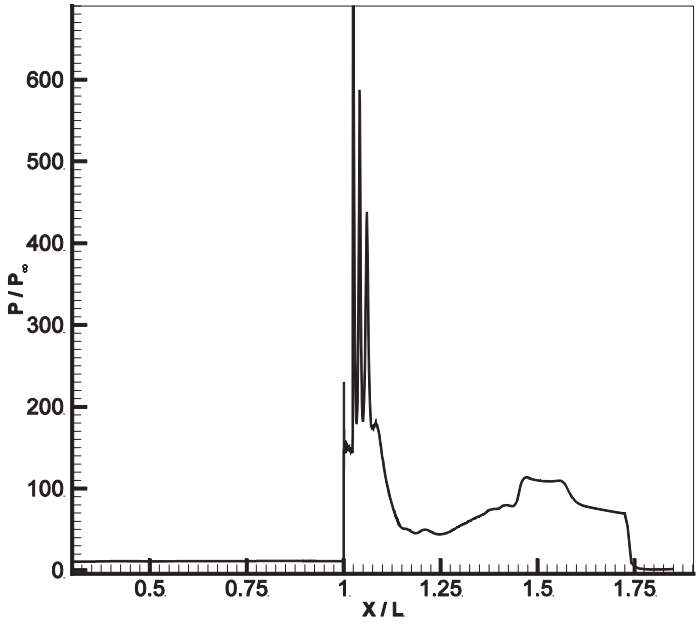

Figure 15. Normalized surface pressure for a seven-shock Type-V interactions with $\theta_2 = 45^0$.

The normalized pressure in all the regions are given in the following table,

Table 2. Computed pressure in different zones in seven-shock Type-V interaction

Region 1	Region 2	Region 3	Region 4	Region5	Region 6	Region 7	Region 8
11.18	144.30	101.50	101.50	358.50	195.20	344.50	650.40

The maximum peak pressure occurs just behind the reflection point of the shock SW2 on the second wedge surface (R_p). The numerical result shows large and rapid variation in the steady- state pressure over the second wedge surface. It is one of the major criteria of Type-IV shock- shock interaction according to Edney's classification. This phenomenon indicates that the interaction is approaching towards the transition from Type-V to Type-IV interaction.

The normalized surface pressure is shown in figure 15. The numerical results show that the maximum surface pressure is around 690. Large changes in quick succession ahead and behind the highest peak is also visible in the surface pressure plot. The first pressure peak occurs due to the shock from the leading edge of the second wedge. This value is 147.2 (shown in the figure 15). Very near to this peak, one more peak occurs just before the highest peak. This peak attains a value of 230. Small amplitude oscillations are observed between the second and the highest peaks.

4 CONCLUSIONS

With the min-mod limiter the code has been able to capture the complex shock-shock interaction patterns quite efficiently. However, it is observed that the oscillations are not adequately controlled when large changes occur successively. Grid plays an important role in this particular gas dynamic problem. It is essential to use properly refined mesh in the shock interaction region near the corner of the double-wedge. The interaction occurs within a very small region; as a result the grid spacing introduces a length scale that determines the resolution required to capture different shock patterns. In this respect, the developed unstructured Euler solver is robust and efficient enough to resolve the present shock interaction problems with comparatively less number of triangular elements. All the simulations in this work are carried out on a mesh with around 0.225 million elements which is about 20% of the structured mesh (1024×1024) used by Olejniczak et al. [6]) for solving the same problem.

Two interaction topologies, namely Type-VI and Type-V and the transition from Type-VI to Type-V are discussed in details. Both six-shock and seven-shock configurations of Type-V interaction are presented. The computed values of normalized pressure in the two regions (1) and (2) for all the cases match reasonably well with the theoretical values. The values of computed normalized pressure for other regions are reasonably good when compared to shock jump relationship. The transition from Type-VI to Type-V occurs when the second wedge angle is between 39.5^0 and 40.0^0. This matches well with the previously calculated value of 39.76^0 (Olejniczak et al. [6]). The different flow topologies and sub-structures of the six-shock and seven-shock types are analyzed in details with the help of numerical results and schematic diagrams.

REFERENCES

[1] Edney, B., Anomalous heat transfer and pressure distribution on blunt bodies at hypersonic speeds in the presence of an impinging shock, *Rep. 115, Flygtekniska Forsoksanstalten (The Aerospace Research Institute of Sweden)*, Stockholm, 1968.

[2] Ben-Dor, G., *Shock Wave Reflection Phenomena*, 2nd Edition, *Springer,* 2007.

[3] Li, H., Chpoun, A. and Ben-Dor, G., Analytical and experimental investigations of the reflection of asymmetric shock waves in steady flows, *J. Fluid Mech.,* 1999, 390, 25-43.

[4] Ivanov, M.S., Ben-Dor, G., Elperin, T., Kudryavtsev, A.N. and Khotyanovsky, D.V., The reflection of asymmetric shock waves in steady flows: a numerical investigation, *J. Fluid Mech.*, 2002, 469, 71-87.

[5] Hu, Z.M., Kim M.S., Myong R.S. and Cho T.H., On the *RR→MR* transition of asymmetric shock waves in steady flows, *Shock Waves*, 2008, 18: 419-423.

[6] Olejniczak, J., Wright, M.J. and Candler, G.V., Numerical study of inviscid shock interactions on double-wedge geometries, *J. Fluid Mech*, 1997, vol. 352, pp. 1-25.

[7] Ben-Dor, G., Vasilev, E. I., Elperin, T. and Zenovich, A.V., Self-induced oscillations in the shock wave flow pattern formed in a stationary supersonic flow over a double wedge, *Physics of Fluids*, 2003, vol. 15, no. 12, pp. L85-L88.

[8] Roe, P.L., Approximate Riemann Solvers, Parameter Vectors, and Difference Schemes, *J. Comput. Phys.,* 1981, 43, pp. 357-372.

[9] Steger, J.L. and Warming, R.F., Flux-Vector splitting of the inviscid gasdynamic equations with application to Finite-Difference Methods, *J. Comput. Phys.,* 1981, 40, pp. 263-293.

[10] van Leer, B., Flux-Vector Splitting for the Euler Equations, *Lecture Notes in Physics,* 1982. 170, pp. 507-512.

[11] Liou, M.S. and Steffen Jr, C.J., A new flux splitting scheme, *J. Comput. Phys*., 1993, 107, pp. 23-39.

[12] Fezoui, L. and Stroufflet, B., A class of implicit upwind schemes for Euler simulations with unstructured meshes, *J. Comput. Phys* , 1989, 84, pp. 174-206.

[13] Liou, M.S., A sequel to AUSM: AUSM+, *J. Comput. Phys*., 1996, 129, pp. 364-382.

[14] Venkatakrishnan, V., A perspective on unstructured grid flow solvers, *NASA Report Number: AD-A292120*, 1995.

[15] Bertolazzi, E. and Manzini, G., A Triangle-based Unstructured Finite Volume Method for Chemically Reactive Hypersonic Flows, *J. Comput. Phys.,* 2001, 166(1), pp. 84-115.

[16] Batina, J.T., Implicit Flux-Split Euler schemes for unsteady aerodynamic analysis involving unstructured dynamic meshes, *AIAA J*., 1991, 29 (11), pp. 1836-1843.

[17] Jameson, A. and Mavriplis, D.J., Finite volume solution of the two-dimensional Euler equations on a regular triangular mesh, *AIAA J*., 1986, 24(4), pp. 611-618.